JACS
JOURNAL OF THE AMERICAN CHEMICAL SOCIETY

Article

pubs.acs.org/JACS

Single-Molecule Catalysis Mapping Quantifies Site-Specific Activity and Uncovers Radial Activity Gradient on Single 2D Nanocrystals

Nesha May Andoy,[†] Xiaochun Zhou, Eric Choudhary, Hao Shen, Guokun Liu, and Peng Chen*

Department of Chemistry and Chemical Biology, Cornell University, Ithaca, New York 14853, United States

Supporting Information

ABSTRACT: Shape-controlled metal nanocrystals are a new generation of nanoscale catalysts. Depending on their shapes, these nanocrystals exhibit various surface facets, and the assignments of their surface facets have routinely been used to rationalize or predict their catalytic activity in a variety of chemical transformations. Recently we discovered that for 1-dimensional (1D) nanocrystals (Au nanorods), the catalytic activity is not constant along the same side facets of single nanorods but rather differs significantly and further shows a gradient along its length, which we attributed to an underlying gradient of surface defect density resulting from their linear decay in growth rate during synthesis (*Nat. Nanotechnol.* **2012**, *7*, 237−241). Here we report that this behavior also extends to 2D nanocrystals, even for a different catalytic reaction. By using super-resolution fluorescence microscopy to map out the locations of catalytic events within individual triangular and hexagonal Au nanoplates in correlation with scanning electron microscopy, we find that the catalytic activity within the flat {111} surface facet of a Au nanoplate exhibits a 2D radial gradient from the center toward the edges. We propose that this activity gradient results from a growth-dependent surface defect distribution. We also quantify the site-specific activity at different regions within a nanoplate: The corner regions have the highest activity, followed by the edge regions and then the flat surface facets. These discoveries highlight the spatial complexity of catalytic activity at the nanoscale as well as the interplay amid nanocrystal growth, morphology, and surface defects in determining nanocatalyst properties.

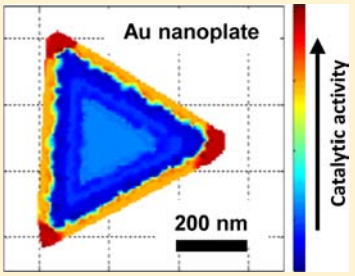

1. INTRODUCTION

Metal nanoparticles are among the most important industrial catalysts.[1−4] They can catalyze a variety of important chemical transformations, including Fischer−Tropsch synthesis, Michael addition, as well as Suzuki- and Heck-coupling reactions.[3−8] The catalytic activity of these nanoparticles is largely defined by the structure of their surfaces, on which the catalysis occurs. Consequently, the catalytic activity of metal nanoparticles is dependent on their shapes,[9−14] as different-shaped nanoparticles present different sets of surface facets and sites; and these facets and sites often differ in activity.[1,15−18] To develop better catalysts, it is important to determine where catalysis occurs and which sites have the highest activity on these nanoparticles.

Advances in the surface science of heterogeneous catalysis have led to a vast amount of knowledge about the catalytic activity of various metal and nonmetal surface sites for a wide range of chemical transformations.[1,7,8,15,19−22] Modern theoretical and computational methods further provide atomistic details about the mechanisms of surface reactions.[7,23,24] As a result, for surfaces of known structure, their catalytic activity can often be predicted from surface science experiments and theory, and one can often rationalize satisfactorily the catalytic activity of different-shaped nanocrystals using the information of their well-defined surface facets.[9−11] However, the surface structure of nanoparticles can be difficult to determine, even for well-faceted metal nanocrystals.[13,14] Measuring the surface catalytic activity of nanocatalysts is thus necessary, where single-particle level measurements are desired, as individual nanocatalysts can differ greatly.[16,25−30] To further differentiate the activity of various surface facets and sites, a most direct way is to measure catalytic reactions in situ on a single nanocatalyst in a spatially resolved manner, which would require quantitative reaction imaging under catalytic conditions and at nanometer resolution.

Electron and X-ray microscopy techniques can image the structure and the chemical nature (e.g., oxidation state) of individual nanoparticles down to nanometer and subnanometer resolution[12,31−36] but lack the ability to quantify activity, i.e., measure reaction kinetics. Scanning probe microscopies can image surface reactions down to the single-molecule level in real time but require flat surfaces and direct contact; they are also difficult to perform under ambient solution conditions.[33−37] Surface plasmon resonance microscopy and spectroscopy can detect catalytic reactions on individual metal nanoparticles[25,29,38] but lack the spatial resolution to resolve subparticle processes.

Single-molecule microscopy of fluorogenic reactions has recently been shown effective to image and quantify catalysis on single catalyst particles down to single-turnover resolution. It has been used to study chemical catalysis on single metal hydroxide catalysts,[39] zeolites,[40] and metal nanoparticles;[41−44] electrocatalysis on clay particles[45] and carbon nanotubes;[46,47]

Received: October 8, 2012
Published: January 15, 2013

   dx.doi.org/10.1021/ja309948y | *J. Am. Chem. Soc.* 2013, 135, 1845−1852

and photocatalysis on TiO_2-based crystals and nanostructures.[28,48−50] The single-molecule fluorescence imaging further enables super-resolution imaging, in which fluorescent reaction products are imaged and localized precisely one at a time to achieve tens of nanometer resolution in resolving catalytic reactions.[51] This super-resolution imaging approach has been used to differentiate catalysis on the different facets of metal hydroxide and oxide microcrystals,[39,52] resolve catalytic domains in porous oxide microneedles/crystals,[53] probe the dimension of reactive sites on carbon-nanotubes,[46] and map plasmonic particle effects on photocatalysis.[50]

In a recent study we have used single-molecule super-resolution fluorescence microscopy to quantitatively image catalysis on single Au nanorods encapsulated in a mesoporous silica shell (i.e., Au@mSiO_2 nanorods), which are pseudo-one-dimensional (1D) nanocrystals.[54] The catalytic reaction was the oxidative N-deacetylation of the nonfluorescent amplex red to the highly fluorescent resorufin by H_2O_2. By localizing each fluorescent product, we obtained catalytic activity maps of individual Au@mSiO_2 nanorods at ∼40 nm resolution. We found complex and surprising spatial catalytic activity patterns on single nanorods; within the same surface facets on the sides of a nanorod, the catalytic reactivity (i.e., the specific catalytic rate constant) not only is nonconstant but also exhibits a gradient from the center of the nanorod toward its two ends. Furthermore, the ratio of the reactivity at the ends of the nanorod to the reactivity at sides varies significantly from nanorod to nanorod, even though they all have the same composition of surface facets. We were able to rationalize these reactivity patterns by using crystal growth-dependent defect density distribution across the surfaces of the nanorods.

To probe if such complex spatial activity pattern exists beyond 1D nanocrystals, here we extend our study to pseudo-2D nanocrystal catalysts, namely, triangular and hexagonal Au nanoplates. Moreover, to diversify the types of catalytic transformations, we study a different fluorogenic catalytic reaction: the reductive N-deoxygenation of resazurin to resorufin by NH_2OH. By correlating super-resolution single-molecule catalysis imaging with scanning electron microscopy (SEM), we find that a 2D radial activity gradient exists on the flat facets of single Au nanoplates, in resemblance to the 1D linear activity gradient we observed on the side facets of single Au nanorods. In addition, we are able to differentiate and quantify directly the catalytic activity at the corner, edge, and facet regions on single Au nanoplates.

2. EXPERIMENTAL SECTION

2.1. Synthesis and Characterization of Au@mSiO_2 Nanoplates. Au nanoplates were synthesized by reducing $AuCl_4^-$ with lemon grass extract, as reported previously.[55] The extract was prepared by boiling 50 g washed and finely cut lemon grass in 250 mL H_2O for 5 min. The light-yellow broth was then cooled to room temperature (rt), and 5 mL of it was added to 45 mL 10^{-3} M $HAuCl_4$. The reaction mixture was incubated overnight at rt and then purified by three cycles of centrifugation at 3000 *g*. The resulting samples were characterized by UV−vis NIR absorption spectroscopy, atomic force microscopy (AFM), and transmission electron microscopy (TEM). The sample contained a mixture of Au nanoplates and pseudospherical nanoparticles, altogether referred to as Au nanoparticles (NPs) hereafter.

The Au NPs were then coated with mesoporous silica as previously reported[54,56−58] (see Section S1 for detailed procedure). The synthesized nanoparticles were first coated with 3-mercaptopropyltrimethoxysilane, and then 0.54% w/v aqueous Na_2SiO_3 solution was used to coat silane-functionalized Au NPs with a thin layer of silica. Further growth of the silica shell was achieved by adding tetraethyl orthosilicate (TEOS) following the Stöber method.[56−58] To make the shell mesoporous, etching with NaOH was done in the presence of CTAB. The resulting Au@mSiO_2 NPs were treated with UV/ozone to remove their organic components (20 W UV lamp illumination in air for ∼12 h at rt), following literature.[59,60] TEM was used to characterize the sample at each step, and it confirmed that the morphology of the Au nanoplates was maintained after coating with silica and UV/ozone treatment (Figure S1). TEM images (Figure 1A) show that the shell

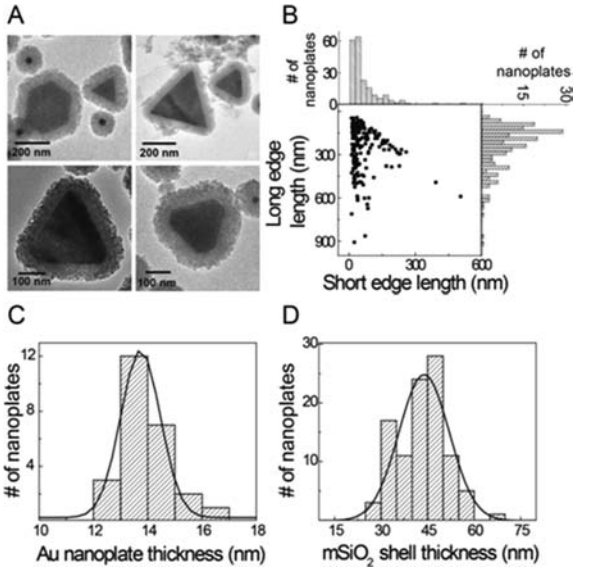

Figure 1. Characterization of Au@mSiO_2 nanoplates. (A) TEM images of triangular and hexagonal Au@mSiO_2. (B) Center: scatter plot of the short vs long edge length of the Au nanoplate cores from TEM. Each dot corresponds to a single nanoplate (total ∼200 nanoplates). Top and right: distributions of the short and long edge lengths. (C) Thickness distribution of the Au nanoplate cores from AFM measurements (Figure S2). Solid line is a Gaussian fit, giving the average thickness of 13.7 ± 0.7 nm. (D) Thickness distribution of the mesoporous silica shell of Au@mSiO_2 nanoplates from TEM. Solid line is a Gaussian fit, giving an average thickness of 43 ± 8 nm.

has complex wormhole-like pores, which, according to literature, have an average pore size of ∼3.5 nm and a specific surface area of ∼1000 m^2 g^{-1}.[58] Ensemble activity assays using UV−vis absorption or fluorescence measurements showed that these Au@mSiO_2 NPs, including the nanoplates, were active in catalyzing the reductive N-deoxygenation of resazurin to resorufin by NH_2OH (Section S2, Figure S3A), consistent with our previous study of uncoated Au NPs.[41−43]

2.2. Single-Molecule Fluorescence Microscopy. Catalysis on individual Au@mSiO_2 nanoplates was imaged using single-molecule total internal reflection fluorescence (TIRF) microscopy as previously described.[41−44] A continuous-wave (∼18−20 mW) circularly polarized 532 nm laser (CrystaLaser) was focused onto an ∼80 × 40 μm^2 area in a microfluidic reactor cell to directly excite the fluorescence of the product resorufin generated on immobilized Au@mSiO_2 nanoplates. The fluorescence was collected by a 60X NA1.2 water-immersion objective (Olympus), filtered, and projected onto an EMCCD camera (Andor) controlled by the Andor IQ software. The time resolution of image acquisition was 22 ms.

The microfluidic reactor cell was formed between a borosilicate coverslip (Gold Seal) and a quartz slide (Technical Glass) separated by double-sided tape. The Au@mSiO_2 nanoplates were dispersed and immobilized on the quartz slide. The slide had micrometer-sized marks etched on its surface via standard photolithography. The slide and coverslip were thoroughly cleaned before assembly. The reaction solution consisted of 50 nM resazurin and 1 mM NH_2OH (Section S2,

Figure S3B), with pH adjusted to 7.3 before it was flowed in at a constant rate of 20 μL min^{-1}.

2.3. Scanning Electron Microscopy (SEM). SEM (LEO 1550VP FESEM operated at 2−5 keV) was done on the same set of Au@$mSiO_2$ nanoplates studied by single-molecule fluorescence microscopy. After fluorescence microscopy measurements, the microfluidic reactor was disassembled, and the slide with the nanoplates was coated with ∼10 nm thick carbon film (Edwards Auto 306 Evaporator). The etched marks on the slide served as guides to locate the area where single-molecule fluorescence movies were taken.

2.4. Super-Resolution Fluorescence Imaging and Correlation with SEM Images. Precise nanometer localizations of catalytic products on individual Au@$mSiO_2$ nanoplates were done as previously described.[54] Briefly, the following steps were performed: (1) extract fluorescence intensity trajectories from individual Au@$mSiO_2$ nanoplates during catalysis, and threshold the trajectories to select fluorescence bursts that come from catalytic product formation reactions; (2) determine the locations (i.e., centroid positions) of individual product molecules by fitting their fluorescence point spread functions (PSFs) with 2D Gaussian function; (3) correct for sample drift using position markers; and (4) remove the noise contribution to the selected fluorescence events via filtering by localization accuracy and width of the fitted PSF.

The locations of product molecules from the fluorescence images were then mapped onto the SEM image of each Au@$mSiO_2$ nanoplate. Specifically, the intrinsic emission[61−63] of the NPs (including both nanoplates and pseudospherical NPs) was imaged and used as markers in the mapping to determine the coordinate transformation relationship between the SEM and fluorescence images. The coordinate transformation was then applied to the locations of all product molecules to map them on top of the SEM image of the NPs; more details in Sections S3−S7.

3. RESULTS AND DISCUSSION

3.1. Catalyst: Au@$mSiO_2$ Nanoplates. Figure 1A shows TEM images of Au nanoplates coated with mesoporous silica shell (i.e., Au@$mSiO_2$ nanoplates). The triangular and hexagonal Au nanoplate cores are single crystals with edge length of about 10−1000 nm (Figure 1B) and thickness of 13.7 ± 0.7 nm (Figure 1C). Their large top and bottom flat surfaces are {111} facets, and the edges are {111} or {110} facets, as assigned previously.[64,65]

The mesoporous silica shell on the Au nanoplates is 43 ± 8 nm thick (Figure 1D). This shell allows us to use UV-ozone treatment to remove the organic ligands on the Au surface for catalysis[59,60] while still maintaining their morphology and preventing their aggregation (Figure S1). The reactants can still access the Au surface for catalysis through the mesopores, and the catalytic kinetics is not limited by the mass transport of the reactants to the Au surface (Section S10). The shell also mimics an oxide support, as is often used in heterogeneous catalysis.[1] Moreover, the mesoporous silica shell helps in trapping the fluorescent product molecules temporarily, facilitating their detection as well as circumventing the potential fluorescence quenching associated with direct detection on Au surfaces.

3.2. Single-Molecule Nanometer Localization of Catalysis on Au@$mSiO_2$ Nanoplates. Our single-molecule imaging of catalysis uses a Au-NP-catalyzed fluorogenic reaction: the reductive N-deoxygenation of the nonfluorescent resazurin to the fluorescent resorufin by NH_2OH in aqueous solution (Figure 2A). To image this reaction on single Au@$mSiO_2$ nanoplates, we immobilized the diluted nanoplates on a quartz slide in a microfluidic reactor cell and supplied the reactants in a constant flow (Figure 2A). Under a total internal reflection fluorescence microscope (Figure 2B), the Au@mSO_2 nanoplates scatter the 532 nm laser light strongly and are also

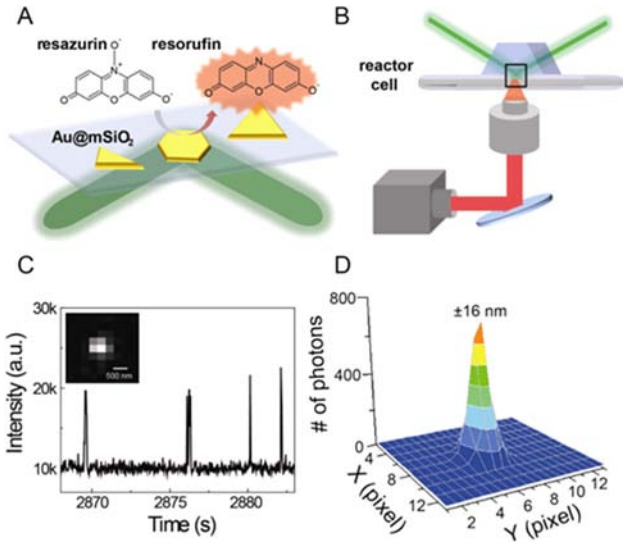

Figure 2. Single-molecule nanometer localization of catalysis on individual Au@$mSiO_2$ nanoplates. (A) Schematic of a microfluidic reactor cell, the TIR laser excitation, and the fluorogenic catalytic reaction. Note that the orientation of the cell here is inversed relative to that in (B); and laser illumination area is not in scale, and it is actually much larger and covers many nanoplates. (B) Schematic of the TIRF microscope. (C) Integrated fluorescence intensity versus time trajectory of a single Au@$mSiO_2$ nanoplate during catalysis ($\langle\tau_{on}\rangle$ = 0.14 s for this trajectory). Inset: fluorescence image of a single resorufin molecule, where the emission signal from the nanoplate was subtracted out. (D) 2D Gaussian fit of the fluorescence image in C inset. The EMCCD signal counts on the *z*-axis have been converted to the actual number of detected photons (Section S4). The center position of this molecule here is localized to ±16 nm.

emissive (Figure S4A),[61−63] making them easily identifiable. Each catalytic reaction generates a fluorescent resorufin molecule, whose laser-induced fluorescence on top of the nanoplate emission signal is imaged on an EMCCD camera. The Au nanoplate cores are sufficiently thin (∼14 nm) to be transparent (∼60% transmittance based on previous measurements of evaporated Au films on glass substrate),[66] and the mesoporous silica shell is also optically transparent (optical transmission is >92%)[67] (Section S4). Therefore, the product molecules on both of the flat facets of the Au nanoplates are excited by the laser and their fluorescence detected.

Figure 2C shows the total fluorescence intensity versus time trajectory from a single Au@$mSiO_2$ nanoplate. It contains intensity bursts on top of a constant Au nanoplate emission signal. Each burst corresponds to one product molecule, i.e., one catalytic turnover, and the duration (i.e., τ_{on}) of each fluorescent burst reports the time each resorufin molecule spends in the shell before it desorbs and disappears into the surrounding solution. The average on-time, $\langle\tau_{on}\rangle$, from all nanoplates is 0.149 ± 0.003 s (error is standard error of the mean).

Figure 2C inset shows the fluorescence image of a single resorufin product, where the emission of the Au nanoplate is subtracted out. Owing to diffraction, the fluorescence signal of a single molecule spreads over a few camera pixels (each pixel ∼267 nm), even though resorufin is only about 1 nm in size. However, if a sufficient number (N) of fluorescence photons are collected, we can localize the center position of the fluorescent molecule to nanometers accuracy by fitting its fluorescence image with a 2D Gaussian function (Figure 2D;

dx.doi.org/10.1021/ja309948y | J. Am. Chem. Soc. 2013, 135, 1845−1852

Section S4). The accuracy of the fit scales approximately with $1/\sqrt{N}$.[68−74] Moreover, since the product molecules do not diffuse significantly (Section S8, Figure S13), they are localized close to where they are catalytically generated. By localizing the positions of fluorescent products one at a time, we were able to map all the product molecules on a single Au@mSiO$_2$ nanoplate.

The fluorescence detection and localization of a molecule in the vicinity of the Au nanoplate can also be affected by the scattering by the nanoplate; this scattering depends on the position and orientation of the molecule with respect to the nanoplate.[75] This could lead to a slight nanometer-scale shift of the fluorescence centroid location as well as a lowering of the fluorescence signal.[75] This, however, will not change the trends of specific activities described in the following sections, as the average orientation of the product molecules with respect to the nanoplate across the many catalytic events is about the same throughout different regions on a nanoplate (Section S4.2), and the shift is small relative to our spatial resolution (∼40 nm, see Section 3.3).

3.3. Spatially Resolved Activity Quantitation on Single Au@mSiO$_2$ Nanoplates. To correlate the locations of catalysis with the structure of Au@mSiO$_2$ nanoplates, we took SEM images of these nanoplates on the same quartz slide used in single-molecule fluorescence imaging experiments (Section S3, Figure S4B). The triangular and hexagonal shapes make these nanoplates easily distinguishable in SEM from the pseudospherical NPs that were also present. The light scattering signal of the marks etched on the slide, and the intrinsic emission of the NPs was used to align the fluorescence images with the SEM images (SSection S3). The locations of product molecules were then mapped onto the SEM image of individual Au@mSiO$_2$ nanoplates (Figure 3A,B, and Figure S7). The spatial uncertainty (ε) of this mapping is ∼40 nm, determined from the relation $\varepsilon^2 = \alpha^2 + \beta^2 + \gamma^2$,[76] which takes into account the resolution of the SEM image (α, ∼25 nm), the average error of localizations of individual product molecules in single-molecule imaging (β, ∼24 nm), and the error of overlaying the fluorescence and SEM images (γ, ∼20 nm) (Section S5).

We then dissected individual Au@mSiO$_2$ nanoplates and the associated product locations into three types of regions: corners, edges, and flat facets (Figure 3A,B). For each Au@mSiO$_2$ nanoplate, the perimeter of its Au nanoplate core was estimated from its SEM structural contour (which outlines the mSiO$_2$ shell) and the average thickness of the silica shell (43 ± 8 nm, Figure 1D). In separating the periphery regions (i.e., corners and edges) from the flat facets, we set the dividing line at 2ε away from the edge of the Au nanoplate core (see Section S6 for details of region dissections). For each type of region(s), we determined its specific activity by counting the number of product molecules per unit time and per Au surface area, where the surface area was based on the model that the Au nanoplates are thin triangular or hexagonal plates with vertical walls (Section S7).[55]

This spatially resolved activity immediately shows that for the two Au@mSiO$_2$ nanoplates, the specific activity follows the trend of corners > edges > flat facets (Figure 3C). When averaged over many Au@mSiO$_2$ nanoplates, either within a group of similar-sized nanoplates or across all (>50 nanoplates), this trend persists with the specific activity of the corner region is ∼8% higher than the edge region, which in turn is ∼80% higher than the flat facet region (Figure 3D).

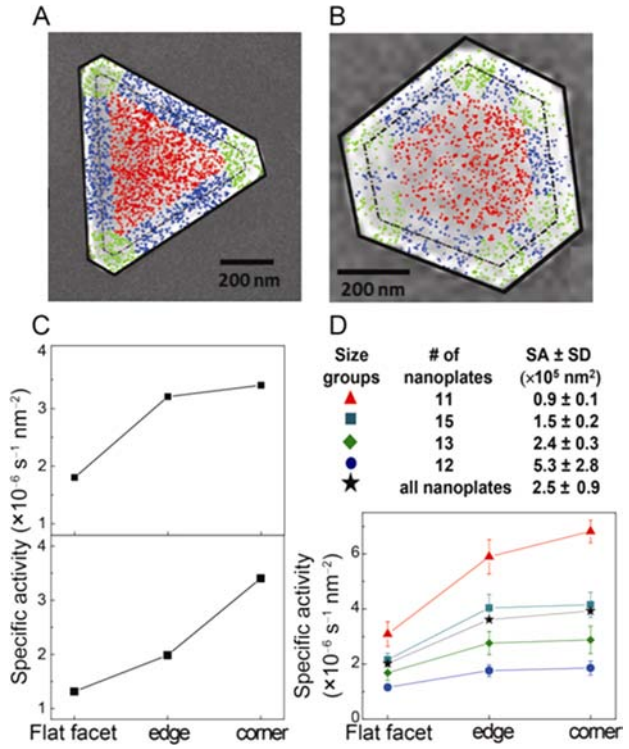

Figure 3. Spatially resolved activity quantitation on single Au@mSiO$_2$ nanoplates. (A) Locations of 2325 product molecules overlaid on top of the SEM image of a Au@mSiO$_2$ nanoplate. Each dot is the location of one product molecule. The locations are color coded according to their respective regions on the nanoplate: flat facet (red), edges (blue), and corners (green). The solid black line outlines the outer contour of the mSiO$_2$ shell. The dashed black line outlines the perimeter of the Au nanoplate core. (B) Same as (A) but for a different Au@mSiO$_2$ nanoplate with 1579 products detected. (C) Specific activities of the different regions of the nanoplates from (A, top) and (B, bottom). (D) Averaged specific activities of different regions on the nanoplates for different size groups (SA = surface area) as well as for all the nanoplates. Error bars are SD.

We also observed that the average time the product molecule stays in the mSiO$_2$ shell (i.e., $\langle\tau_{on}\rangle$) has a slight region dependence: $\langle\tau_{on}\rangle_{corners} < \langle\tau_{on}\rangle_{edges} < \langle\tau_{on}\rangle_{facets}$, although the differences are small (Figure S15). Since the distributions of τ_{on} follow exponential decays (Figure S16) and our time resolution is limited (22 ms), the fraction of product molecules that we can detect is relatively higher in the flat facet regions than in the edges and corners. If we correct for these differences in detection fraction by using the distributions of τ_{on} (details in Section S11), the trend in specific activity that we observed remains the same and becomes even more pronounced: Corners are ∼13% higher in specific activity than edges, which in turn are ∼90% higher than flat facets.

The relative specific activity of different regions can be readily rationalized provided that the catalytic sites are low-coordination metal sites (e.g., corner, edge, and defect sites), which are often more reactive due to their coordination unsaturation.[1,11] Recent work by Katz et al.[77] on the same reaction system further supports that the reactive sites are low-coordination sites. The percentage of available low-coordination surface sites generally follows the trend of corner > edge > flat facet regions, thus giving rise to the corresponding trend in specific activity. The trend is also consistent with our previous study of Au@mSiO$_2$ nanorods,[54] whose ends are in general

higher in activity than their side facets in catalyzing an oxidative N-deacetylation reaction, even though we study a different, i.e., a reductive N-deoxygenation, reaction here for the Au@mSiO$_2$ nanoplates.

3.4. Size and Shape Dependence of Site-Specific Activity. We further examined how the specific activities of corner, edge, and flat facet regions of Au@mSiO$_2$ nanoplates are correlated with the nanoplates' size and shape. Figure 4A shows how the specific activity of these three types of regions depends on the surface area (which is a measure of the size) of the Au nanoplate core. The specific activities of all regions, as well as that of whole nanoplates, show a gradual decrease with increasing nanoplate surface area. Past studies have shown that for NPs of > ~2 nm in diameter, the size-dependent specific activity can be rationalized using a classic thermodynamic model invoking the NPs' size-dependent chemical potential (for details see our previous work).[43] In this model, the specific activity scales approximately with $e^{1/d}$ and thus with $e^{1/\sqrt{A}}$, where d is the particle diameter and A is the surface area; therefore, the specific activity would decrease with increasing particle size, consistent with our observations. Using this model, we fitted the size-dependent specific activities (v) of different regions with the relation $v = v_\infty \exp(a/\sqrt{A})$, where parameter a quantifies the extent of the size dependence (Figure 4A). When $A \rightarrow \infty$, $v = v_\infty$; thus v_∞ represents the specific activity of bulk Au. The fitted values of a are similar for all regions (about 200 nm), consistent with the model that the size dependences of their specific activities come from the same thermodynamic origin. The values of v_∞ are close to zero, consistent with that bulk Au has negligible activity in catalyzing the reductive N-deoxygenation of resazurin.[41]

Figure 4B plots the specific activities of Au@mSiO$_2$ nanoplates against their long vs short edge length ratio, a measure of their shape being more triangular or hexagonal. To factor out the size effect, the specific activity of each region was normalized with respect to its expected activity according to its size (Figure 4A and Section S7). There is no significant dependence within experimental error on the nanoplate shape for the specific activity of either the whole nanoplate (Figure 4B) or any type of regions (Figure S12). This lack of shape dependence is not surprising since these Au nanoplates share the same types of surface facets regardless of being triangular or hexagonal.

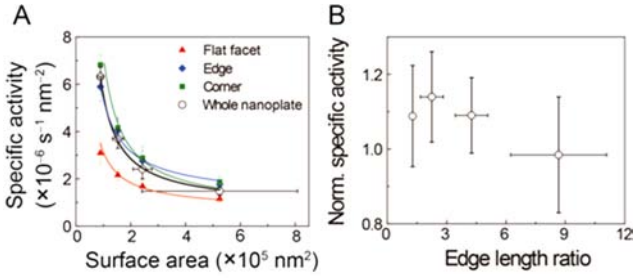

Figure 4. (A) Size dependences of the specific activities of different regions as well as the nanoplate as a whole particle. Each data point is an average of similar-sized nanoplates. The solid lines are fits with $v = v_\infty \exp(a/\sqrt{A})$ (A = surface area), where a(flat facet) = (1.8 ± 3.5) × 10^2 nm, a(edge) = (1.8 ± 0.1) × 10^2 nm, a(corner) = (2.7 ± 3.7) × 10^2 nm, and a(whole nanoplate) = (2.3 ± 0.1) × 10^2 nm; and v_∞(flat facet) = (5 ± 14) × 10^{-7} s^{-1} nm^{-2}, v_∞(edge) = (9 ± 1) × 10^{-7} s^{-1} nm^{-2}, v_∞(corner) = (5 ± 12) × 10^{-7} s^{-1}nm^{-2}, and v_∞(whole nanoplate) = (5.6 ± 0.4) × 10^{-7} s^{-1} nm^{-2}. (B) The specific activity against the long vs short edge length ratio of Au@mSiO$_2$ nanoplates. Each data point is an average of similar-shaped nanoplates. The specific activities are normalized by the size (i.e., surface area) of the nanoplates (Section S7). Error bars are SD for x-axis and standard error of the mean for y-axis.

3.5. Radial Gradient of Activity on the Flat {111} Facet. We further dissected the {111} flat facets of single, relatively larger, Au@mSiO$_2$ nanoplates into radial segments and examined whether the catalytic activity would be uniform or not within the same surface facet (Figure 5A). Each radial segment has a width of ε (the spatial uncertainty in our SEM/optical correlation, ~40 nm, see Section 3.3), except for the center segment, which has a radius of 2ε from the geometric center of the nanoplate (Section S6). Strikingly, the specific activities of these segments on a single nanoplate show a clear radial gradient, highest at the center of the facet and decaying toward the periphery (Figure 5B), even though they are within the same {111} surface facet. This radial activity gradient in the flat facets persists even after correcting for the events that were not detected due to limited time resolution (Section S11, Figures S18 and S19).

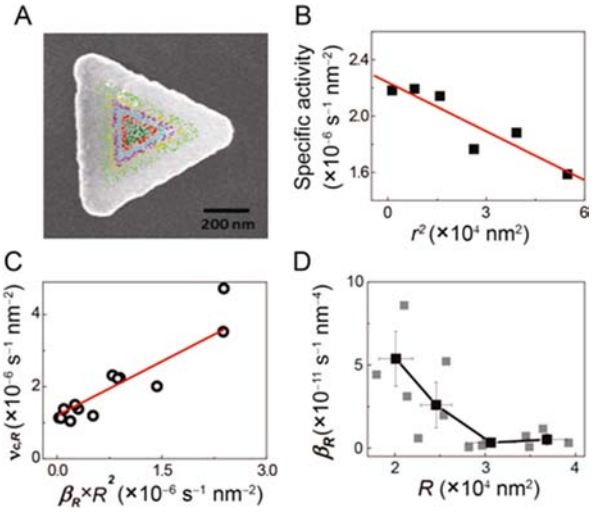

Figure 5. Radial gradient of specific activity on the {111} facets of Au@mSiO$_2$ nanoplate. (A) Locations of ~1055 product molecules overlaid on top of the SEM image of a Au@mSiO$_2$ nanoplate (same as the one in Figure 3A). The facets (i.e., top and bottom) are divided into radial segments from the center toward the periphery; the product locations in different segments are colored differently. The product molecules residing in the corner and edge regions are excluded here. (B) Dependence of specific activities of radial segments on r^2 for the nanoplate in (A), where r is the distance between the center of the nanoplate and the midpoint of the segment along the center-to-corner vector, as defined in Section S9. Solid line is a fit with eq 1. (C) Linear correlation between $v_{c,R}$ and $\beta_R R^2$ of individual nanoplates. Each point is from one nanoplate. The red line is a linear fit with a slope of 1 and y-intercept of (1.2 ± 0.1) × 10^{-6} s^{-1} nm^{-2}. (D) Correlation of the radial activity gradient β_R with R of the nanoplates. The gray solid squares are from individual nanoplates. The black solid circles are binned averages.

We have previously observed an activity gradient on single Au@mSiO$_2$ nanorods, which are pseudo-1D nanocrystals.[54] Along the length of a single nanorod, the activity decays from its center toward its two ends, attributable to its underlying surface defect density gradient that resulted from the nanorod's

dx.doi.org/10.1021/ja309948y | J. Am. Chem. Soc. 2013, 135, 1845−1852

linear decay in growth rate when the nanorod grew from a seed during synthesis.[78] Past studies have shown that the Au nanoplates are likely formed via 2D seeded growth, i.e., starting from a seed particle and then growing in 2D into a plate.[55,79−82] As the growth rate must decrease over time for the nanoplate to stop growing eventually (because of, e.g., depletion of reactants), we propose that the radial activity gradient of Au nanoplates results from a similar cause: the flat {111} facets of the nanoplate have an underlying radial gradient of surface defect density that comes from the decaying 2D growth rate when the nanoplate grows from a seed.

Based on this proposal and assuming the catalytic activity, reflected by the specific turnover rate $v_R(r)$, at a radial distance r from the center of a nanoplate of radius R, is linearly proportional to the local surface defect density, which in turn is linearly proportional to the nanoplate 2D growth rate at that location, we have the following (Section S9):

$$v_R(r) = -\beta_R r^2 + v_{c,R} \quad (1)$$

Both r and R are distances measured along the nanoplate center-to-corner vector (Figure S14). The parameter β_R is the radial activity gradient from the center of the nanoplate toward the periphery; it also reflects the underlying gradient of defect density and that of the growth rate, where $v_{c,R}$ is the activity at the nanoplate center. This quantitative model based on our proposal also dictates $v_{c,R} = \beta_R R^2 + v_0$ for each nanoplate; here v_0 represents the specific activity of the nanoplate flat facet when its 2D growth rate approaches zero (note it is not the nanoplate edge/corner but close to it), i.e., a perfect {111} facet. Using eq 1 to fit data as in Figure 5B, we obtained β_R and $v_{c,R}$ for every nanoplate. Putting together the results from many nanoplates, we observed a linear correlation between $v_{c,R}$ and $\beta_R R^2$ with a slope of ∼1 (Figure 5C). The experimental verification of this predicted linear correlation validates our model based on our proposal. Moreover, y-intercept of this linear correlation gives v_0 ∼1 × 10^{-6} s^{-1} nm^{-2}, the activity of perfect top facets under our reaction conditions.

The nanoplate size dependence of β_R further provides new insights into the growth of these Au nanoplates during synthesis. The larger the nanoplate (i.e., bigger R), the smaller β_R is (Figure 5D), indicating a shallower gradient of activity from the center toward the periphery on the {111} facets. Based on our proposal, this shallower activity gradient suggests a slower decay of their 2D growth rates during synthesis for the larger nanoplates. The slower decay of their growth rate contributes to the larger nanoplates' being eventually larger.

The discovery of spatial catalytic activity gradients within the same crystal facets on pseudo-2D nanocrystals (i.e., Au nanoplates) in this study, as well as on pseudo-1D nanocrystals (i.e., Au nanorods) studied previously, has implications in studying and understanding the catalytic activity of nanocrystal catalysts. This discovery reinforces the importance of surface defects in determining the catalytic properties of metal surfaces, as well-studied in surface science of heterogeneous catalysis.[1,83,84] For shape-controlled colloidal nanocrystals, for which facet information is often used to explain activity, it is challenging to determine their surface defects, but it is imperative to consider them, so one could better use the knowledge from surface science to understand their activities. Structural studies, such as electron or X-ray microscopy,[31,85] in conjunction with single-molecule super-resolution catalysis imaging of shape-controlled nanocrystals, should offer a powerful approach to help understand and develop better catalysts.

4. CONCLUSION

We have used single-molecule super-resolution fluorescence microscopy, coupled with electron microscopy, to study the site-specific activity on single $mSiO_2$-coated 2D Au nanoplates in catalyzing a reductive N-deoxygenation reaction. We directly visualize that the specific activity of different regions on a single nanoplate follows the trend of corner regions > edge regions > flat surface facet regions, indicating that the reactive sites are mainly low-coordination metal sites. In addition, within the flat surface facets of each nanoplate, we observe a 2D radial gradient in activity from the center toward the edges. We propose a model of underlying surface defect density gradient to explain the observed activity gradient. This model is consistent with the trend of specific activity among corners, edges, and flat facets and also quantitatively fits our experimental results satisfactorily. Along with our earlier discovery on pseudo-1D Au nanorods, these results show that complex activity patterns within single crystal facets are not limited to 1D nanocrystals but are also true for 2D nanocatalysts and in different catalytic transformations. These discoveries corroborate the importance of surface defects in catalysis long-learned from surface science of heterogeneous catalysis as well as stress the need to examine in detail the surface structure of shape-controlled nanocrystals besides their surface facet assignments in understanding their catalytic behaviors.

■ ASSOCIATED CONTENT

Ⓢ Supporting Information

Detailed procedures of catalyst synthesis and characterization; single-molecule imaging experiments; SEM and fluorescence image correlation; detailed procedures of dissecting individual nanoplates; control experiments; and derivation of the radial activity gradient model. This material is available free of charge via the Internet at http://pubs.acs.org/.

■ AUTHOR INFORMATION

Corresponding Author

pc252@cornell.edu

Present Address

[†]Department of Cell Biology, Harvard Medical School, Boston, MA 02115, and Program in Cellular and Molecular Medicine, Children's Hospital, Boston, MA 02115.

Notes

The authors declare no competing financial interest.

■ ACKNOWLEDGMENTS

This research is mainly supported by the Department of Energy (DE-FG02-10ER16199), with partial support from the Army Research Office (W911NF0910232) and National Science Foundation [CBET-0851257 (P.C.), DGE0903653 (E.C.)]. Part of the work was done at the Cornell Center for Materials Research (DMR-0520404) and Cornell NanoScale Facility (ECS-0335765). We thank Jiwoong Park and Michael Segal for providing some of the quartz slides with etched position marks.

■ REFERENCES

(1) Somorjai, G. A.; Li, Y. *Introduction to Surface Chemistry and Catalysis*; 2nd ed.; John Wiley & Sons: Hoboken, NJ, 2010.

(2) Ertl, G.; Knözinger, H.; Weitkamp, J. *Handbook of heterogeneous catalysis*; VCH: Weinheim, 1997.
(3) *Nanoparticles and Catalysis*; Astruc, D., Ed.; Wiley-VCH: Weinheim, 2007.
(4) Crooks, R. M.; Zhao, M.; Sun, L.; Chechik, V.; Yeung, L. K. *Acc. Chem. Res.* **2001**, *34*, 181.
(5) Jia, C.-J.; Schuth, F. *Phys. Chem. Chem. Phys.* **2011**, *13*, 2457.
(6) Li, Y.; Hong, X. M.; Collard, D. M.; El-Sayed, M. *Nano Lett.* **2000**, *2*, 2385.
(7) Zope, B. N.; Hibbitts, D. D.; Neurock, M.; Davis, R. J. *Science* **2010**, *330*, 74.
(8) Somorjai, G. A.; Contreras, A. M.; Montano, M.; Rioux, R. M. *Proc. Natl. Acad. Sci. U.S.A.* **2006**, *103*, 10577.
(9) Burda, C.; Chen, X.; Narayanan, R.; El-Sayed, M. A. *Chem. Rev.* **2005**, *105*, 1025.
(10) Xia, Y.; Xiong, Y.; Lim, B.; Skrabalak, S. E. *Angew. Chem., Int. Ed.* **2009**, *48*, 60.
(11) Lee, H.; Habas, S. E.; Kweskin, S.; Butcher, D.; Somorjai, G. A.; Yang, P. *Angew. Chem., Int. Ed.* **2006**, *45*, 7824.
(12) Murphy, C. J.; Thompson, L. B.; Chernak, D. J.; Yang, J. A.; Sivapalan, S. T.; Boulos, S. P.; Huang, J.; Alkilany, A. M.; Sisco, P. N. *Curr. Opin. Colloid Interface Sci.* **2011**, *16*, 128.
(13) Carbó-Argibay, E.; Rodríguez-González, B.; Gómez-Graña, S.; Guerrero-Martínez, A.; Pastoriza-Santos, I.; Pérez-Juste, J.; Liz-Marzán, L. M. *Angew. Chem., Int. Ed.* **2010**, *49*, 9397.
(14) Katz-Boon, H.; Rossouw, C. J.; Weyland, M.; Funston, A. M.; Mulvaney, P.; Etheridge, J. *Nano Lett.* **2011**, *11*, 273.
(15) Ertl, G. *Reactions at Solid Surfaces*; John Wiley & Sons, Inc.: Hoboken, NJ, 2009.
(16) Weckhuysen, B. M. *Angew. Chem., Int. Ed.* **2009**, *48*, 4910.
(17) Narayanan, R.; El-Sayed, M. A. *J. Phys. Chem. B* **2005**, *109*, 12663.
(18) Tao, A. R.; Habas, S.; Yang, P. *Small* **2008**, *4*, 310.
(19) Goodman, D. W. *Chem. Rev.* **1995**, *95*, 523.
(20) Liu, X.; Madix, R. J.; Friend, C. M. *Chem. Soc. Rev.* **2008**, *37*, 2243.
(21) Thompson, T. L.; Yates, J. T., Jr. *Chem. Rev.* **2006**, *106*, 4428.
(22) Kim, H.; Kosuda, K. M.; Van Duyne, R. P.; Stair, P. C. *Chem. Soc. Rev.* **2010**, *39*, 4820.
(23) Nilsson, A.; Pettersson, L. G. M.; Norskov, J. K. *Chemical Bonding at Surfaces and Interfaces*; Elsevier: Amsterdam, 2008.
(24) van Santen, R. A.; Neurock, M.; Shetty, S. G. *Chem. Rev.* **2010**, *110*, 2005.
(25) Novo, C.; Funston, A. M.; Mulvaney, P. *Nat. Nanotechnol.* **2008**, *3*, 598.
(26) Cremer, G. D.; Sels, B. F.; Vos, D. E. D.; Hofkens, J.; Roeffaers, M. B. J. *Chem. Soc. Rev.* **2010**, *39*, 4703.
(27) Chen, P.; Zhou, X.; Shen, H.; Andoy, N. M.; Choudhary, E.; Han, K.-S.; Liu, G.; Meng, W. *Chem. Soc. Rev.* **2010**, *39*, 4560.
(28) Tachikawa, T.; Majima, T. *Chem. Soc. Rev.* **2010**, *39*, 4802.
(29) Liu, N.; Tang, M. L.; Hentschel, M.; Giessen, H.; Alivisatos, A. P. *Nat. Mater.* **2011**, *10*, 631.
(30) Tao, F. F.; Salmeron, M. *Science* **2011**, *331*, 171.
(31) Zheng, H.; Smith, R. K.; Jun, Y.-W.; Kisielowski, C.; Dahmen, U.; Alivisatos, A. P. *Science* **2009**, *324*, 1309.
(32) Zheng, H.; Rivest, J. B.; Miller, T. A.; Sadtler, B.; Lindenberg, A.; Toney, M. F.; Wang, L.-W.; Kisielowski, C.; Alivisatos, A. P. *Science* **2011**, *333*, 206.
(33) Meier, J.; Friedrich, K. A.; Stimming, U. *Faraday Discuss.* **2002**, *121*, 365.
(34) Lai, S. C. S.; Dudin, P. V.; Macpherson, J. V.; Unwin, P. R. *J. Am. Chem. Soc.* **2011**, *133*, 10744.
(35) Ebejer, N.; Schnippering, M.; Colburn, A. W.; Edwards, M. A.; Unwin, P. R. *Anal. Chem.* **2010**, *82*, 9141.
(36) Chen, S.; Kucernak, A. *J. Phys. Chem. B* **2004**, *108*, 13984.
(37) Hulsken, B.; Hameren, R. V.; Gerritsen, J. W.; Khoury, T.; Thordarson, P.; Crossley, M. J.; Rowan, A. E.; Nolte, R. J. M.; Elemans, J. A. A. W.; Speller, S. *Nat. Nanotechnol.* **2007**, *2*, 285.
(38) Tang, M. L.; Liu, N.; Dionne, J. A.; Alivisatos, A. P. *J. Am. Chem. Soc.* **2011**, *133*, 13220.
(39) Roeffaers, M. B.; Sels, B. F.; Uji-i, H.; De Schryver, F. C.; Jacobss, P. A.; De Vos, D. E.; Hofkens, J. *Nature* **2006**, *439*, 572.
(40) Roeffaers, M. B. J.; Sels, B. F.; Uji-i, H.; Blanpain, B.; L'Hoëst, P.; Jacobs, P. A.; De Schryver, F. C.; Hofkens, J.; De Vos, D. E. *Angew. Chem., Int. Ed.* **2007**, *46*, 1706.
(41) Xu, W.; Kong, J. S.; Yeh, Y.-T. E.; Chen, P. *Nat. Mater.* **2008**, *7*, 992.
(42) Xu, W.; Kong, J. S.; Chen, P. *Phys. Chem. Chem. Phys.* **2009**, *11*, 2767.
(43) Zhou, X.; Xu, W.; Liu, G.; Panda, D.; Chen, P. *J. Am. Chem. Soc.* **2010**, *132*, 138.
(44) Han, K. S.; Liu, G.; Zhou, X.; Medina, R. E.; Chen, P. *Nano Lett.* **2012**, *12*, 1253.
(45) Lei, C.; Hu, D.; Ackerman, E. *Nano Lett.* **2009**, *9*, 655.
(46) Xu, W.; Shen, H.; Kim, Y. J.; Zhou, X.; Liu, G.; Park, J.; Chen, P. *Nano Lett.* **2009**, *9*, 3968.
(47) Shen, H.; Xu, W.; Chen, P. *Phys. Chem. Chem. Phys.* **2010**, *12*, 6555.
(48) Tachikawa, T.; Majima, T. *Langmuir* **2012**, *28*, 8933.
(49) Tachikawa, T.; Majima, T. *Chem. Commun.* **2012**, *48*, 3300.
(50) Tachikawa, T.; Yonezawa, T.; Majima, T. *ACS Nano* **2013**, *7*, 263.
(51) Roeffaers, M. B.; De Cremer, G.; Uji-i, H.; Muls, B.; Sels, B. F.; Jacobs, P. A.; De Schryver, F. C.; De Vos, D. E.; Hofkens, J. *Proc. Natl. Acad. Sci. U.S.A.* **2007**, *104*, 12603.
(52) Tachikawa, T.; Yamashita, S.; Majima, T. *J. Am. Chem. Soc.* **2011**, *133*, 7197.
(53) Roeffaers, M. B. J.; Cremer, G. D.; Libeert, J.; Ameloot, R.; Dedecker, P.; Bons, A.-J.; Buckins, M.; Martens, J. A.; Sels, B. F.; De Vos, D. E.; Hofkens, J. *Angew. Chem., Int. Ed.* **2009**, *48*, 9285.
(54) Zhou, X.; Andoy, N. M.; Liu, G.; Choudhary, E.; Han, K.-S.; Shen, H.; Chen, P. *Nat. Nanotechnol.* **2012**, *7*, 237.
(55) Shankar, S. S.; Rai, A.; Ankamwar, B.; Singh, A.; Ahmad, A.; Sastry, M. *Nat. Mater.* **2004**, *3*, 482.
(56) Liz-Marzán, L. M.; Giersig, M.; Mulvaney, P. *Langmuir* **1996**, *12*, 4329.
(57) Stöber, W.; Fink, A.; Bohn, E. *J. Colloid Interface Sci.* **1968**, *26*, 62.
(58) Botella, P.; Corma, A.; Navarro, M. T. *Chem. Mater.* **2007**, *19*, 1979.
(59) Aliaga, C.; Park, J. Y.; Yamada, Y.; Lee, H. S.; Tsung, C.-K.; Yang, P.; Somorjai, G. A. *J. Phys. Chem. C* **2009**, *113*, 6150.
(60) Vig, J. *J. Vac. Sci. Tech. A* **1985**, *3*, 1027.
(61) Geddes, C. D.; Parfenov, A.; Gryczynski, I.; Lakowicz, J. R. *Chem. Phys. Lett.* **2003**, *380*, 269.
(62) Tcherniak, A.; Dominguez-Medina, S.; Chang, W.-S.; Swanglap, P.; Slaughter, L. S.; Landes, C. F.; Link, S. *J. Phys. Chem. C* **2011**, *115*, 15938.
(63) He, H.; Xie, C.; Ren, J. *Anal. Chem.* **2008**, *80*, 5951.
(64) Grzelczak, M.; Pérez-Juste, J.; Mulvaney, P.; Liz-Marzán, L. M. *Chem. Soc. Rev.* **2008**, *37*, 1783.
(65) Millstone, J. E.; Park, S.; Shuford, K. L.; Qin, L.; Schatz, G. C.; Mirkin, C. A. *J. Am. Chem. Soc.* **2005**, *127*, 5312.
(66) Smith, G. B.; Niklasson, G. A.; Svensson, J. S. E. M.; Granqvist, C. G. *J. Appl. Phys.* **1986**, *59*, 571.
(67) Bae, J. Y.; Suk-Ho, Choi; Byeong-Soo, Bae *Bull. Korean Chem. Soc.* **2006**, *27*, 1562.
(68) Thompson, R. E.; Larson, D. R.; Webb, W. W. *Biophys. J.* **2002**, *82*, 2775.
(69) Yildiz, A.; Forkey, J. N.; McKinney, S. A.; Ha, T.; Goldman, Y. E.; Selvin, P. R. *Science* **2003**, *300*, 2061.
(70) Qu, X.; Wu, D.; Mets, L.; Scherer, N. F. *Proc. Nat. Acad. Sci.* **2004**, *101*, 11298.
(71) Thompson, M. A.; Biteen, J. S.; Lord, S. J.; Conley, N. R.; Moerner, W. E. *Methods Enzymol.* **2010**, *475*, 27.

(72) Betzig, E.; Patterson, G. H.; Sougrat, R.; Lindwasser, O. W.; Olenych, S.; Bonifacino, J. S.; Davidson, M. W.; Lippincott-Schwartz, J.; Hess, H. F. *Science* **2006**, *313*, 1642.
(73) Hess, S. T.; Girirajan, T. P. K.; Mason, M. D. *Biophys. J.* **2006**, *91*, 4258.
(74) Rust, M. J.; Bates, M.; Zhuang, X. *Nat. Methods* **2006**, *3*, 793.
(75) Lin, H.; Centeno, S. P.; Su, L.; Kenens, B.; Rocha, S.; Sliwa, M.; Hofkens, J.; Uji-i, H. *ChemPhysChem* **2012**, *13*, 973.
(76) Grunwald, D.; Singer, R. H. *Nature* **2010**, *467*, 604.
(77) Nigra, M. M.; Arslan, I.; Katz, A. *J. Catal.* **2012**, *295*, 115.
(78) Gulati, A.; Liao, H.; Hafner, J. H. *J. Phys. Chem. B* **2006**, *110*, 22323.
(79) Klajn, R.; Pinchuk, A. O.; Schatz, G. C.; Grzybowski, B. A. *Angew. Chem., Int. Ed.* **2007**, *46*, 8363.
(80) Ha, T. H.; Koo, H.-J.; Chung, B. H. *J. Phys. Chem. C* **2006**, *111*, 1123.
(81) Wang, C.; Kan, C.; Zhu, J.; Zeng, X.; Wang, X.; Li, H.; Shi, D. *J. Nanomater.* **2010**, 969030.
(82) Zhan, G.; Ke, L.; Li, Q.; Huang, J.; Hua, D.; Ibrahim, A.-R.; Sun, D. *Ind. Engr. Chem. Res.* **2012**, *51*, 15753.
(83) Yates, J. T. *J. Vac. Sci. Technol., A* **1995**, *13*, 1359.
(84) Wallace, W. T.; Min, B. K.; Goodman, D. W. *J. Mol. Catal. A* **2005**, *228*, 3.
(85) de Smit, E.; Swart, I.; Creemer, J. F.; Hoveling, G. H.; Gilles, M. K.; Tyliszczak, T.; Kooyman, P. J.; Zandbergen, H. W.; Morin, C.; Weckhuysen, B. M.; de Groot, F. M. F. *Nature* **2008**, *456*, 222.